Evaluation of Downward Shortwave Radiation Products Over the Loess Plateau

Qianqian Tian, Shuhua Zhang, Weili Duan, and Guanghui Ming

***Abstract*—Downward shortwave radiation (DSR) is a key component of the surface energy budget, influencing atmospheric circulation and climate change. DSR products derived from remote sensing observations or generated from reanalysis systems are commonly used as inputs for ecohydrological and climate models. The Loess Plateau is severely affected by soil erosion and has experienced frequent extreme weather events in recent years. Therefore, an accurate DSR product is crucial for accurately simulating climate change and surface-atmosphere processes on the Loess Plateau. In this study, newly released satellite DSR products CLouds, Albedo and Radiation Edition 3 data (CLARA-A3) and Moderate Resolution Imaging Spectroradiometer land surface Downward Shortwave Radiation Version 6.1 data (MCD18A1 V6.1), along with the reanalysis product Land component of the Fifth Generation European Centre for Medium-Range Weather Forecasts Reanalysis (ERA5-Land), were evaluated over the Loess Plateau and its surrounding areas. Intraday, daily, monthly, and seasonal DSR were evaluated against ground measurements which were collected from five observation networks. CLARA-A3 outperformed MCD18A1 and ERA5-Land on both monthly and daily scales. The root-mean-square error for monthly (daily) DSR from CLARA-A3, ERA5-Land, and MCD18A1 were 19.31 (31.3) W/m^2, 25.36 (39.74) W/m^2, and 25.03 (46.14) W/m^2, respectively. The study explored potential factors contributing to significant errors in DSR products. Results indicated that snow cover was one possible factor influencing the error in MCD18A1, and CLARA-A3 exhibited greater sensitivity to terrain influence compared to ERA5-Land and MCD18A1. The findings can be the reference for selecting DSR products over the Loess Plateau.**

***Index Terms*—Downward shortwave radiation (DSR), Loess Plateau, reanalysis, remote sensing.**

I. Introduction

DOWNWARD shortwave radiation (DSR) is the portion of solar radiation after the absorption, reflection, and scattering of atmosphere particles. It is an important component of the surface radiation and energy budget and is also the fundamental driving force of the climate system and ecohydrological processes [1], [2]. DSR is also shown as solar energy. As the clean energy, it is very beneficial to the environment and climate. Therefore, DSR is crucial to climate change, ecohydrological processes, and solar energy utilization on the Earth's surface [3], [4], [5].

Ground station is the traditional and accurate way for DSR observation [6], [7], but the sparsity and heterogeneity of ground stations show limited spatial representation [8]. With the development and progress of remote sensing technology, DSR retrieved from satellite observations represent high temporal and spatial continuity [9]. DSR satellite products are usually generated based on polar orbit satellites or a combination of polar orbit and geostationary satellites, including Moderate Resolution Imaging Spectroradiometer land surface Downward Shortwave Radiation dataset (MCD18A1), and CLouds, Albedo and Radiation Edition 3 data (CLARA-A3) generated from AVHRR sensor and International Satellite Cloud Climatology Project - H-Series Product (ISCCP-H) which was mainly produced by AVHRR, VISSR, and VAS sensors [10]. There are region-specific products such as shortwave radiation products from Himawari-8, GOES-R, and Fengyun (FY) series satellites. In addition, the reanalysis system that was the fusion of model and observation data produces long-term products [11], such as Modern-Era Retrospective Analysis for Research and Applications V2 (MERRA2), Land component of the Fifth Generation European Centre for Medium-Range Weather Forecasts Reanalysis (ERA5-Land). Satellite or reanalysis DSR products both have been used as input in ecohydrological or climatic models. However, these products show high uncertainty due to the ways that they are generated. Satellite DSR products from different satellite platforms have different accuracies affected by observation methods, observation periods, and retrieval methods [12], [13], [14], [15], [16]. Data sources and assimilation schemes for the reanalysis data are diverse and input datasets (such as clouds and aerosols) of the assimilation process and model tend to cause systematic errors in the reanalysis DSR products [17], [18]. Therefore, understanding the uncertainty and error of satellites and reanalysis DSR products is a prerequisite before they are used as reasonable variables in applications.

We collected research about error assessment of reanalysis and satellite DSR products in different spatial scopes, i.e., global, China, and local region and they are shown in Table I . Summarizing the assessments in Table I, it shows larger error for reanalysis datasets than satellite datasets with monthly DSR, especially

Manuscript received 6 November 2023; revised 6 December 2023; accepted 12 December 2023. Date of publication 22 December 2023; date of current version 18 January 2024. This work was supported by the National Natural Science Foundation of China under Grant 42122004, Grant 42001219, Grant 41977059, and Grant 41701442. *(Corresponding author: Shuhua Zhang.)*

Qianqian Tian and Shuhua Zhang are with the College of Geomatics, Xi'an University of Science and Technology, Xi'an 710054, China (e-mail: qiantian@stu.xust.edu.cn; shuhuazhang@xust.edu.cn).

Weili Duan is with the State Key Laboratory of Desert and Oasis Ecology, Xinjiang Institute of Ecology and Geography, Chinese Academy of Sciences, Urumqi 830011, China (e-mail: duanweili@ms.xjb.ac.cn).

Guanghui Ming is with the Key Laboratory of Water Management and Water Security for Yellow River Basin, Ministry of Water Resources, Yellow River Engineering Consulting Company Ltd., Zhengzhou 450003, China (e-mail: minggh@yrec.cn).

Digital Object Identifier 10.1109/JSTARS.2023.3346032

TABLE I
COLLECTIONS OF RESEARCH ABOUT ERROR ASSESSMENT OF REANALYSIS AND SATELLITE DSR PRODUCTS

Coverage	Spatial resolution	Type	Organization	Product	Observation network	Evaluation result	Reference
Global	Monthly	Reanalysis	NCEP	NCEP-NCAR /NCEP-DOR/CFSR	GEBA, BSRN, GC-NET, NOAA, CMA.	MBE: 18.57 ─ 49.80 RMSE: 32.23 ─ 59.97	Zhang et al. [18]
			ECMWF	ERA-Interim	GEBA, BSRN, GC-NET, NOAA, CMA.	MBE: 11.25 RMSE: 27.7	
			NOAA	MERRA	GEBA, BSRN, GC-NET, NOAA, CMA.	MBE: 22.36 RMSE: 34.13	
		Satellite	GEWEX	GEWEX-SRB V3.0	GEBA	MBE: 8.1 RMSE: 24.1	Zhang et al. [31] Zhang et al. [19] Ma et al. [32]
			GISS	ISCCP-FD	GEBA/BSRN	MBE: 8.7/2.0 RMSE: 28.7	
			UMD	UMD-SRB V3.3.3	GEBA/BSRN	MBE: 10.9/-0.6 RMSE: 24.0/13.1	
			CERES	CERES-EBAF	GEBA, BSRN, GC-NET, NOAA, CMA.	MBE: 3.33 RMSE: 17.98	Zhang et al. [18]
	Daily	Satellite	CERES	CERES-SYN	FLUXNET, SURFRAD, GC-NET, FMI, NIBIO.	MBE: 2.2 RMSE: 27.6	Wang et al. [15] Li et al. [20]
			NASA	MCD18A1	(FLUXNET, SURFRAD, GC-NET, FMI, NIBIO)/BSRN	MBE: -7.8 ─ -8 RMSE: 31.6 ─ 32.3	
			High-resolution products	BESS, GLASS-DSR, CLARA-A2	FLUXNET, SURFRAD, GC-NET, FMI, NIBIO	MBE: -8 ─ -1.5 RMSE: 29.1 ─ 30.3	
China	Monthly	Reanalysis	NCEP	NCEP-NCAR /NCEP-DOR/ CFSR/CFSv2	CMA	MBE: 26.9 ─ 71.95 RMSE: 39.0 ─ 79.03	Zhang et al. [18] Zhang et al. [22] Zhang et al. [21] Tong et al. [33] Jia et al. [23]
			ECMWF	ERA-Interim/ ERA5	CMA/DAM/CERN/TPDC	MBE: 13.2 ─ 25.1 RMSE: 28.43 ─ 37.1	
			NOAA	MERRA/ MERRA2	CMA/DAM/CERN/TPDC	MBE: 29.9 ─ 43.84 RMSE: 41.1 ─ 45.76	
		Satellite	GEWEX	GEWEX-SRB V3.0	CMA	MBE: 8.9─14.6 RMSE: 22.9─25.9	Zhang et al. [19] Wu et al. [34]
			CERES	CERES-SYN /CERES-EBAF	CMA	MBE: 5.3 ─ 8.1 RMSE: 20.0 ─ 20.5	
			NSMC	FY-2C	CMA	MBE: 3.5 RMSE: 31.9	Zhang et al. [22] Zhang et al. [19]
			NASA	MCD18A1	CERN, TPDC	MBE: -7.31 RMSE: 23.44	Jia et al. [23] Tong et al. [33]
			High-resolution products	BESS, GLASS-DSR, CLARA-A2	CERN, TPDC	MBE: -2.32 ─ 1.85 RMSE: 15.94─20.56	
	Daily	Reanalysis	ECMWF	ERA-Interim/ERA5	CMA/CERN	MBE: 14.1 ─ 16.58 RMSE: 41.01 ─ 48.2	Zhang et al. [22] Tong et al. [33]
			NOAA	MERRA2	CMA/CERN	MBE: 31.5─33.91 RMSE: 57.6─61.2	
		Satellite	GEWEX	GEWEX-SRB V3.0	CMA	MBE: 6.5 RMSE: 39.07	Zhang et al. [19] Jia et al. [23] Tong et al. [33]
			NSMC	FY-2C	CMA	MBE: 3 RMSE: 49.3	
			NASA	MCD18A1	CERN, TPDC	MBE: -6.58 RMSE: 37.11	
			High-resolution products	BESS, GLASS-DSR, CLARA-A2	CERN, TPDC	MBE: -1.42 ─ 2.65 RMSE: 30.24─35.7	
	1-h	Reanalysis	ECMWF	ERA5	CMA/CERN	MBE: 30.87 RMSE: 120.56─155.52	Jiang et al. [35] Tong et al. [33]
			NOAA	MERRA2	CERN	MBE: 184.91 RMSE: 256.07	
Tibetan Plateau	Monthly	Satellite	GEWEX	GEWEX-SRB	GAME-Tibet	MBE: -48 RMSE: 50	Yang et al. [24]
			GISS	ISCCP-FD	GAME-Tibet	MBE: -10 RMSE: 17	
	Daily	Reanalysis	NOAA	MERRA	CMA	MBE: 3.67	Wang et al. [26]
			ECMWF	ERA-Interim	CMA	MBE: 1.78	
	3-h	Satellite	GEWEX	GEWEX-SRB V2.5/V2.81	GAME-Tibet	MBE: -16.5 ─ -49	Yang et al. [25]
			GISS	ISCCP-FD	GAME-Tibet	MBE: -11.9	
			UMD	UMD-SRB	GAME-Tibet	MBE: -0.9	

Note: The units of MBE and RMSE are W/m^2. The full names of acronyms are shown in Appendix TABLE VI.

TABLE II
DETAILS OF DSR SATELLITE PRODUCTS AND REANALYSIS PRODUCTS

Product	Spatial resolution	Temporal resolution	Temporal coverage	Data sources
CLARA-A3	0.25°(~25km)	Monthly/Daily	1979.01–Present	https://wui.cmsaf.eu
ERA5-Land	0.1°(~10km)	Monthly/1-h	1950.01–Present	https://cds.climate.copernicus.eu
MCD18A1	1 km	3-h/Instantaneous	2000.01–Present	https://search.earthdata.nasa.gov

datasets from National Centers for Environmental Prediction (NCEP) that shows larger error among all reanalysis datasets [18], [19]. Among different satellite DSR datasets, DSR from the Clouds and the Earth's Radiant Energy System (CERES) show relatively small errors than other satellite datasets [18], [19]. Meanwhile, the daily CERES DSR dataset also presents a relatively larger error than the monthly DSR [18], [20]. These characters can be found in global and China on monthly and daily scales [18], [19], [21], [22]. For regional DSR product evaluation, the Tibetan Plateau has attracted much attention due to its unique geographical location and climate [24], [25], [26], [27]. DSR products show relatively larger errors over the Tibetan Plateau because of its high reliefs and complex environment [25], [27]. Loess Plateau, its underlying surface show high spatial heterogeneity with land cover changing from forest to desert from south to north. The climate over the Loess Plateau shows a transition followed by semiarid, semihumid, and arid regions from south to north [28]. Land cover and its specific climate both influence solar radiation by changing the surface albedo and atmosphere attenuation processes, respectively. The Loess Plateau is also the region most severely affected by soil erosion, and it has experienced frequent extreme weather events in recent years [29], [30]. An accurate shortwave radiation (solar radiation) product is crucial for accurately simulating climate change or surface-atmosphere processes on the Loess Plateau. Therefore, a comprehensive assessment of DSR products over Loess Plateau is necessary for selecting suitable products in applications. In this study, newly released satellite DSR products of MCD18A1 V6.1 and CLARA-A3, and reanalysis DSR product of ERA5-Land form ECMWF were evaluated in different time scales (i.e., intraday, daily, monthly, and seasonal) on the Loess Plateau. These three products feature higher resolutions than existing DSR products and are newly updated. We also analyzed temporal trend consistency and discussed the error sources for different DSR products. The evaluation results can provide more detailed information for the selection of DSR products in various applications on the Loess Plateau.

II. DATA AND METHOD

A. Data

1) CLARA-A3: The CLARA-A3 data is the latest edition of the CLARA data record which provides cloud properties and surface radiation parameters derived from the AVHRR sensor onboard the series of polar-orbiting NOAA satellites and METOP satellites [16]. It was published by the European Organization for the Exploitation of Meteorological Satellites (EUMETSAT) Satellite Application Facility on Climate Monitoring (CM SAF) in 2023. It covers globally and has a spatial resolution with 0.25° × 0.25°. The time span of the dataset is from 1979 to 2023. The retrieval algorithm of DSR used in the generation of the CLARA-A3 data record is based on a look-up-table (LUT) approach by Mueller et al. [36]. Compared to version 2, CLARA-A3 has improved its applicability in ice and snow-covered regions by replacing constant surface albedo data with temporally varying surface albedo data. The details of DSR products used in this study are shown in Table II.

2) ERA5-Land: ERA5-Land is a newly released reanalysis dataset by ECMWF. ERA5-Land is a replay of the land component of the ERA5 climate reanalysis, forced by meteorological fields from ERA5 [37]. H-TESSEL is the land surface model that is the basis of ERA5-Land. ERA5-Land has been currently providing hourly reanalysis data since 1950. To some extent, the ERA5-Land dataset could be the first hourly dataset for describing energy balances at a spatial resolution of 0.1° on global land surface for more than 70 years, which makes this dataset very useful for land surface applications.

3) MCD18A1 (Version 6.1): MCD18A1 is a Level 3 product of the DSR mainly generated by the senor of Moderate Resolution Imaging Spectroradiometer (MODIS) on Terra and Aqua satellite. MCD18A1 provides data from 2000 to the present at a 1 km spatial resolution and 3-h/instantaneous temporal resolutions. This product uses MODIS L1b top-of-atmosphere reflectance, MCD43A3 surface albedo, MERRA2 water vapor products, GTOPO30 DEM, and MODIS geolocation as the input data of the look-up table method to calculate DSR [15].

4) Ground Stations: To evaluate the accuracy of DSR products, ground measurements were collected from five networks in the Loess Plateau and its surrounding areas: four sites from the Chinese Ecosystem Research Network (CERN), 17 sites from the China Meteorological Administration (CMA), five sites from the Network Observation System for Key Ecological Processes on the Loess Plateau (NOLP), nine sites from Heihe Integrated Observatory Network (HION), and one site in Suide that was installed by our research team. The instrument used at the Suide is a CMP10 solar radiation sensor produced by Kipp & Zonen. The elevations of these sites range from 110 to 4148 m, and were evenly distributed in the study area, as shown in Fig. 1. The details of ground stations used in this study are shown in Table III.

B. Methodology

1) Quality Control of the Ground Measurements: High-quality ground measurements are the prerequisite for the accurate evaluation of products. To screen out high-quality ground measurements, the quality control procedure applied in this article consists of the following two steps based on the work presented by Li et al. [20].

TABLE III
DETAILS OF GROUND STATIONS

Network	Number	Temporal resolution	Temporal coverage	Data sources
CERN	4	Monthly/daily/hourly	2016.01–2020.12	http://cnern.org.cn
NOLP	5	Monthly	2020.01–2020.12	http://loess.geodata.cn
CMA	17	Daily	2000.03–2017.12	http://data.cma.cn
HION	9	10-min	2014.01–2022.12	http://www.tpdc.ac.cn
Suide	1	1-min	2020.08–2022.12	\

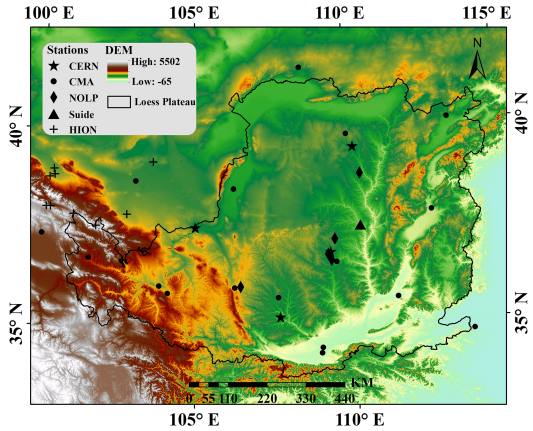

Fig. 1. Geographical distribution of the observation stations.

Step 1: For subhour measurements, we set the DSR values that had a negative solar elevation angle to 0.

Step 2: We applied range quality control procedures based on extremely rare limits test of BSRN [38]. For different temporal resolutions, range-quality control procedures are operated as follows [39]:

Monthly and daily:

$$0.03\mathrm{GHI}_{\mathrm{toa}} < \mathrm{GHI} < \mathrm{GHI}_{\mathrm{toa}}. \tag{1}$$

Hourly and subhourly:

$$0.03\mathrm{GHI}_{\mathrm{toa}} < \mathrm{GHI} < 1.2I_0 \cos\left(\mathrm{SZA}\right)^{1.2} + 50 \tag{2}$$

where GHI is the global horizontal irradiance, $\mathrm{GHI}_{\mathrm{toa}}$ is the global horizontal irradiance at the top of atmosphere (TOA), I_0 is the normal irradiance at the TOA, and SZA is the solar zenithal angle. They are calculated using the following formula:

$$\mathrm{GHI}_{\mathrm{toa}} = I_0 \cos(\mathrm{SZA}) \tag{3}$$

$$I_0 = I_{\mathrm{sc}} E_0 \tag{4}$$

where I_{sc} is the solar constant (approximately 1367 W/m^2), and E_0 is the Earth orbit eccentricity correction factor, calculated by

$$E_0 = 1.00011 + 0.034221\cos\Gamma + 0.00128\sin\Gamma + 0.000719\cos 2\Gamma + 0.000077\sin 2\Gamma \tag{5}$$

where Γ, in radians, is called the day angle. It is calculated by

$$\Gamma = 2\pi\left(\frac{d_n - 1}{365}\right) \tag{6}$$

where d_n represents the day number of the year, ranging from 1 on January 1st to 365 (or 366) on December 31st. For the leap year, 365 can be replaced by 366.

The $\cos(\mathrm{SZA})$ is calculated by

$$\cos(\mathrm{SZA}) = \sin\delta\sin\phi + \cos\delta\cos\phi\cos\omega \tag{7}$$

where δ, in degrees, is the solar declination angle, ϕ is the station latitude, ω is the hour angle that is 0 at noon, positive in the morning, and changes 15° per hour. δ is calculated by

$$\delta = 23.45\sin\left(360\frac{d_n + 284}{365}\right) \tag{8}$$

2) Data Aggregation: The temporal resolutions of the DSR products evaluated in this study are instantaneous (MCD18A1), 1-h (ERA5-Land), 3-h (MCD18A1), daily (CLARA-3), and monthly (ERA5-Land and CLARA-3). Temporal resolutions of ground measurements are 1-min (Suide station), 10-min (HION), 1-h (CERN), daily (CERN and CMA), and monthly (CERN and NOLP). Therefore, it is necessary to aggregate the data temporally to address the inconsistency in temporal resolution between DSR products and ground measurements.

Due to the absence of daily and monthly scale DSR products from MCD18A1, a temporal aggregation procedure is employed to obtain data at these scales. Daily-scale data are derived by averaging eight 3-h data intervals within a day, whereas monthly-scale data are obtained by averaging the aggregated daily DSR. Although ERA5-Land products do not directly provide daily-scale products, their hourly data represents the cumulative values from 00:00 of the day to the respective hour, with the data at "00:00" representing the daily data from the preceding day.

For the ground measurements, a three-step temporal aggregation process is implemented. First, subhourly DSR was aggregated into hourly DSR. Due to interrupting from the instrument itself or environment, the observed dataset was filled with "No data" in some times. We excluded these values. If the number of available observations for 1-min temporal resolution within an hour is more than 30, or more than 3 for 10-min temporal resolution, all available DSR is averaged within that hour to produce the hourly DSR. The second step, we aggregated hourly DSR into daily DSR. Typically, daily DSR was directly averaged by valid hourly DSR. However, days with more missing hourly DSR may underestimate daily DSR. We adopted the hourly-to-daily aggregation method proposed by Li et al. [20], where the hourly DSR within a day is divided into eight intervals and more than two valid observed data in each interval was considered as "valid interval." In total, 8 "valid interval" was used to aggregate daily DSR. Finally, monthly DSR was aggregated based on valid daily DSR when 25 or more valid daily DSR was within each month.

Furthermore, to evaluate the accuracy of products at a seasonal scale, we divided all months into four seasons as follows: MAM represents March, April, and May. JJA represents June, July, and

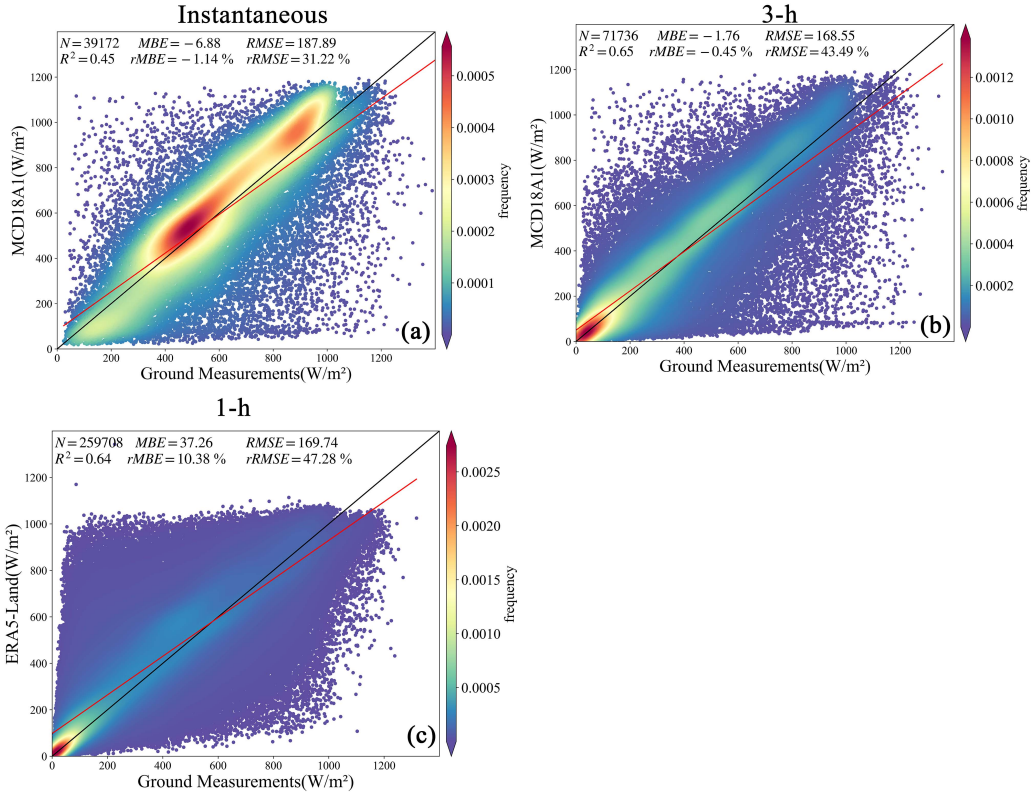

Fig. 2. Validation of the instantaneous and 3-h MCD18A1 DSR and 1-h ERA5-Land DSR against ground measurements. (a) Instantaneous DSR of MCD18A1. (b) 3-h DSR of MCD18A1. (c) 1-h DSR of ERA5-land. Black line: 1:1 line. Red line: Fitted regression line.

August. SON represents September, October, and November. DJF represents December, January, and February.

C. Evaluation Indicator

We calculated the accuracy of products by comparing DSR over pixel with the ground observation that is located in the corresponding pixel directly. We used the following metrics to evaluate the performance of DSR products.

The coefficient of determination (R^2): The magnitude of R^2 determines the degree of correlation. Its values range from 0 to 1, with values closer to 1 indicating a higher consistency between products and ground measurements. (9) shown at the bottom of this page, where e_i is the value of products, m_i is the value of ground measurements, and n is the number of samples.

Root mean square error (RMSE) and relative RMSE (rRMSE): used to represent the overall deviation.

$$\mathrm{RMSE} = \sqrt{\frac{\sum_{i=1}^{n}(e_i - m_i)^2}{n}} \tag{10}$$

$$\mathrm{rRMSE} = \frac{\mathrm{RMSE}}{\frac{1}{n}\sum_{i=1}^{n} m_i}. \tag{11}$$

Mean bias error (MBE) and relative MBE (rMBE): used to represent the real deviation between observed DSR and products. A positive deviation represents an overestimation of the DSR by the satellite or reanalysis product, and a negative deviation represents an underestimation of the DSR by the satellite or reanalysis product.

$$\mathrm{MBE} = \frac{\sum_{i=1}^{n}(e_i - m_i)}{n} \tag{12}$$

$$\mathrm{rMBE} = \frac{\mathrm{MBE}}{\frac{1}{n}\sum_{i=1}^{n} m_i}. \tag{13}$$

D. Temporal Trend Analysis Method

Sen's slope estimation method and the Mann–Kendall trend test were employed to analyze temporal trend characteristics and consistency between three DSR products and ground measurements. To eliminate the impact of seasonal variations on the DSR temporal trend, the temporal trend evaluation was performed on DSR anomalies (the DSR time series was deseasonalized by subtracting the long-term average seasonal effects from the monthly values).

$$R^2 = \sqrt{\frac{\left(n\sum_{i=1}^{n} e_i m_i - \sum_{i=1}^{n} e_i \times \sum_{i=1}^{n} m_i\right)^2}{\left[n\sum_{i=1}^{n} e_i^2 - \left(\sum_{i=1}^{n} e_i\right)^2\right] \times \left[n\sum_{i=1}^{n} m_i^2 - \left(\sum_{i=1}^{n} m_i\right)^2\right]}} \tag{9}$$

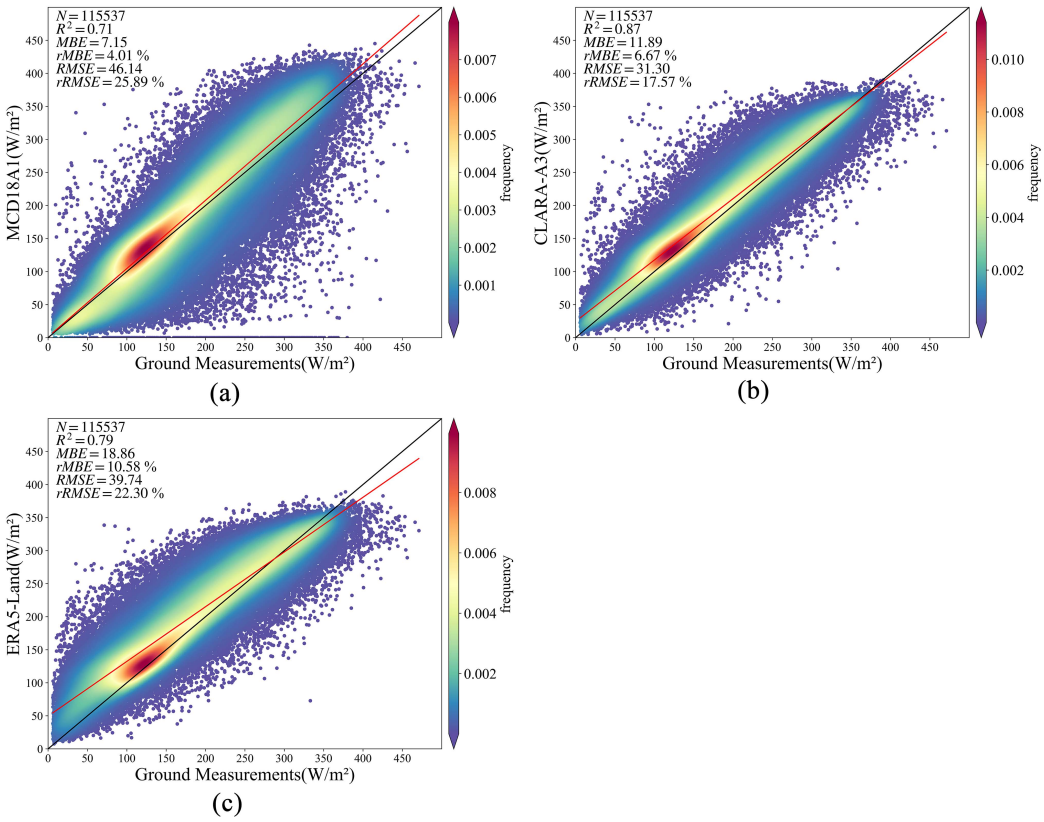

Fig. 3. Validation of daily DSR products against ground measurements. (a) MCD18A1. (b) CLARA-A3. (c) ERA5-land. Black line: 1:1 line. Red line: Fitted regression line.

Sen's slope estimation is a robust trend calculation method, where the slope (θ) represents the average rate of change and trend in time series. A positive θ indicates an upward trend, θ equaling 0 indicates no obvious trend, and a negative θ indicates a downward trend. Furthermore, the larger θ, the more pronounced the trend. The calculation formula is

$$\theta = Median\left(\frac{x_j - x_k}{j-k}\right) \forall j > k \tag{14}$$

where $Median$ is the median function, x_j and x_k are the DSR anomalies for index values j and k, and$j > k$.

Mann–Kendall trend test is a nonparametric statistical test, which has been widely used in the trend test and analysis of long time series data. The standardized test statistic (Z) is calculated as follows:

$$Z = \begin{cases} \frac{S-1}{\sqrt{Var(S)}}, & \text{if } S > 0 \\ 0, & \text{if S} = 0 \\ \frac{S+1}{\sqrt{Var(S)}}, & \text{if } S < 0 \end{cases} \tag{15}$$

where $Var(S)$ is the variance of S, and S is the test statistic, calculated by

$$S = \sum_{k=1}^{t-1} \sum_{j=k+1}^{t} sign(x_j - x_k) \tag{16}$$

$$sign(x_j - x_k) = \begin{cases} 1, & \text{if } (x_j - x_k) > 0 \\ 0, & \text{if } (x_j - x_k) = 0 \\ -1, & \text{if } (x_j - x_k) < 0 \end{cases} \tag{17}$$

where t is the number of time series samples.

III. Results and Analysis

A. Intraday DSR

MCD18A1 had provided instantaneous DSR for each individual MODIS overpass and 3-h DSR. ERA5-Land had provided 1-h DSR. The ground measurements collected from the HION, CERN, and Suide were employed for the validation of intraday data. The validation procedure was conducted at the original resolution of MCD18A1 and ERA5-Land and validation results are shown in Fig. 2. For MCD18A1 [see Fig. 2(a) and (b)], both the instantaneous and 3-h data exhibited negative MBE of -6.88 W/m^2 (-1.14%) and -1.76 W/m^2 (-0.45%), respectively. The rRMSE of instantaneous and 3-h DSR were 31.22% and 43.49%. It shows that the errors of 3-h DSR for MCD18A1 are larger than the instantaneous DSR. The possible reason is that 3-h DSR of MCD18A1 is obtained through temporal interpolation and the instantaneous data is acquired based on instantaneous scan at overpass time. When atmospheric conditions vary significantly within a day, the temporal interpolation process may not accurately capture these changes, leading to increased uncertainty in 3-h DSR. The MBE and RMSE of ERA5-Land 1-h DSR [see Fig. 2(c)] were 37.26 W/m^2 (10.38%) and 169.74 W/m^2 (47.28%).

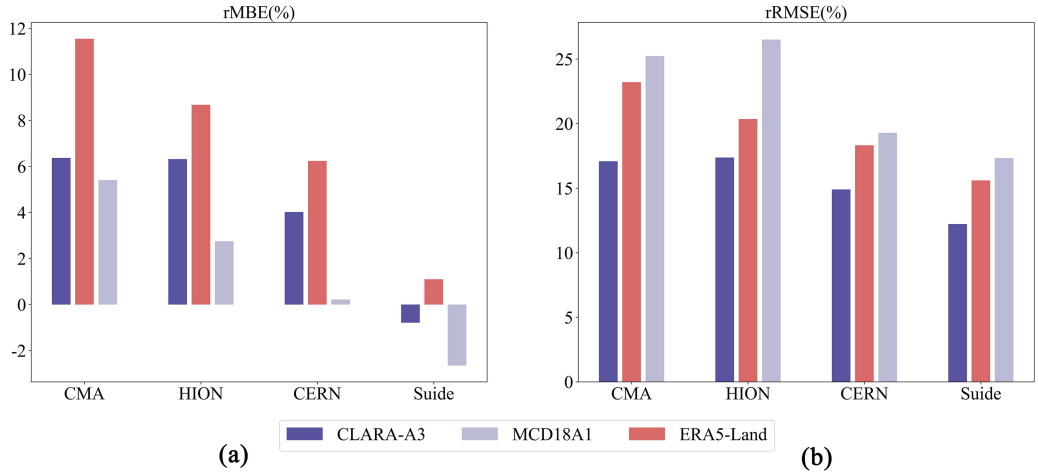

Fig. 4. Comparison of daily DSR rMBE and rRMSE over different networks. (a) rMBE. (b) rRMSE.

B. Daily DSR

The ground measurements used to assess the accuracy of the daily-scale products are collected from four observation networks: CMA, CERN, HION, and Suide. A consistent comparison of CLARA-A3, ERA5-Land, and MCD18A1 was conducted based on a spatial resolution of 0.25°. As shown in Fig. 3, the MBEs of the daily DSR products were 7.15 W/m^2 (4.01%), 11.89 W/m^2 (6.67%), and 18.86 W/m^2 (10.58%) for MCD18A1, CLARA-A3, and ERA5-Land, respectively. It reveals an overestimation of the three daily DSR products in the Loess Plateau. The RMSEs of the daily DSR products were 46.14 W/m^2 (25.89%), 31.30 W/m^2 (17.57%), 39.74 W/m^2 (22.30%) for MCD18A1, CLARA-A3 and ERA5-Land, respectively, which indicate that CLARA-A3 performs best among three products. By comparing the error assessment of Tong et al. [33] over China, we can find that RMSE of MCD18A1 daily DSR in Loess Plateau (46.14 W/m^2) is higher than that in China where the RMSE is 37.11 W/m^2. It indicates that regional assessments for DSR datasets are necessary for local applications. Fig. 4 shows the comparison of daily DSR products over different networks. CLARA-A3 demonstrates the highest level of agreement on the CMA and HION networks, with differences in rRMSE and rMBE of 0.28% and 0.05%, respectively.

C. Monthly DSR

The ground measurements used to assess the accuracy of the monthly-scale products are collected from all sites within the five observation networks in this study. The spatial resolutions of ERA5-Land and MCD18A1 were both resampled to 0.25° to match the CLARA-A3 for a more consistent comparison. As shown in Fig. 5, the MBEs of the monthly DSR products were 6.22 W/m^2 (3.51%), 10.46 W/m^2 (5.89%), and 17.66 W/m^2 (9.95%) for MCD18A1, CLARA-A3, and ERA5-Land, respectively. It also reveals an overestimation of the three monthly DSR products in the Loess Plateau. The RMSEs of the monthly DSR products were 25.03 W/m^2 (14.11%), 19.31 W/m^2 (10.89%), and 25.36 W/m^2 (14.30%) for MCD18A1, CLARA-A3, and ERA5-Land, respectively. The CLARA-A3 exhibits the best performance, whereas the ERA5-Land and MCD18A1 show relatively similar performance. The RMSE of MCD18A1 monthly DSR in Loess Plateau (25.03 W/m^2) is higher than that in China where the RMSE is 23.44 W/m^2 based on Tong et al. [33].

Fig. 6 shows the comparison of monthly DSR products over different networks. The evaluation results that CLARA-A3 has the highest accuracy while ERA5-Land has the lowest accuracy are consistent in CMA, CERN, and NOLP. Compared to MCD18A1 and CLARA-A3, ERA5-Land overestimates significantly on CMA and CERN, with rMBE of 11.27% and 9.45%, respectively. This is consistent with previous research findings, indicating that reanalysis data tends to overestimate DSR [18], [22]. For the HION network, the rRMSE of CLARA-A3 and MCD18A1 are 13.33% and 17.00%, respectively. The rRMSE of ERA5-Land is 12.54%, which is lower than the other two satellite products. This may be due to all sites of the HION network being located in the Heihe River Basin where the terrain is complex (shown in Fig. 1), with three sites having elevations exceeding 3600 m. It is also influenced by snow cover. Therefore, the influence of snow cover and terrain on the products is discussed in Section IV.

D. Seasonal DSR

Fig. 7 shows the evaluation results of the seasonal DSR of three products using ground measurements. Comparing the rRMSE of three products at all seasons, we found that the error of CLARA-A3 was the lowest in MMA, JJA, and SON, which indicates that CLARA-A3 performed better with relatively low rRMSE. ERA5-Land and MCD18A1 had similar accuracy in MMA, JJA, and SON with differences in rRMSE of 0.37%, 0.24%, and 0.44%, respectively. In different seasons, the rRMSE was the lowest in JJA and the highest in DJF for all products. Previous studies have suggested that the uncertainty of DSR products in snow-covered regions may increase, which could be a possible reason for the lower accuracy in DJF [18], [33].

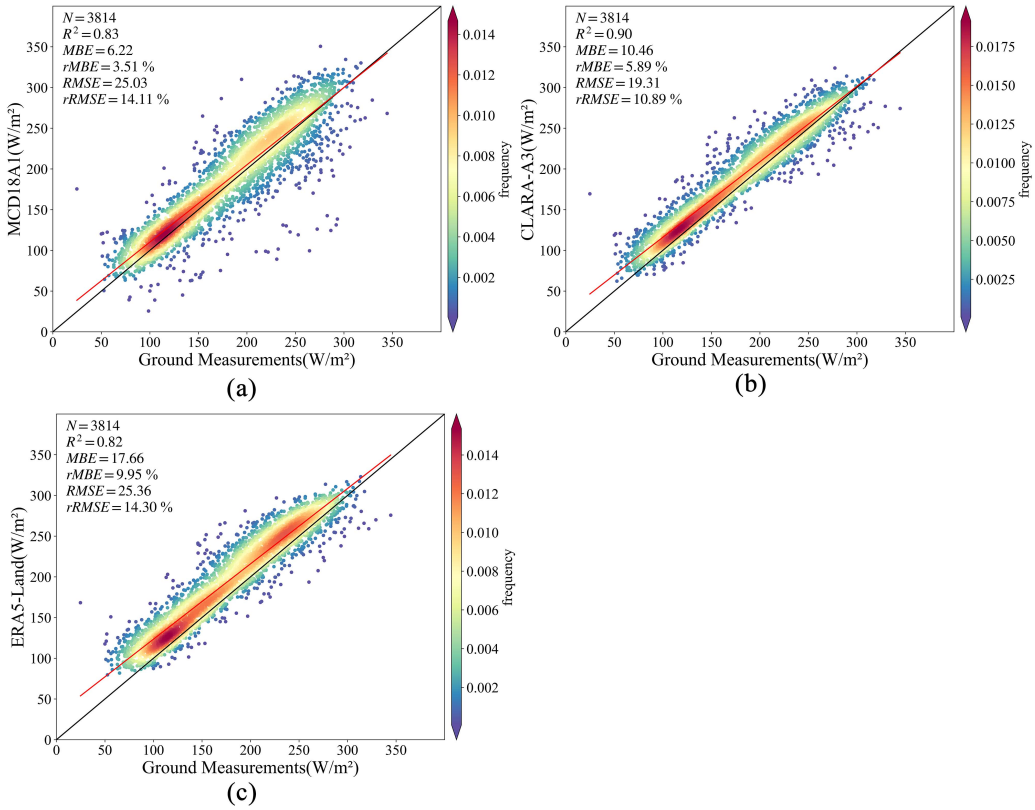

Fig. 5. Validation of monthly DSR products against ground measurements. (a) MCD18A1. (b) CLARA-A3. (c) ERA5-land. Black line: 1:1 line. Red line: Fitted regression line.

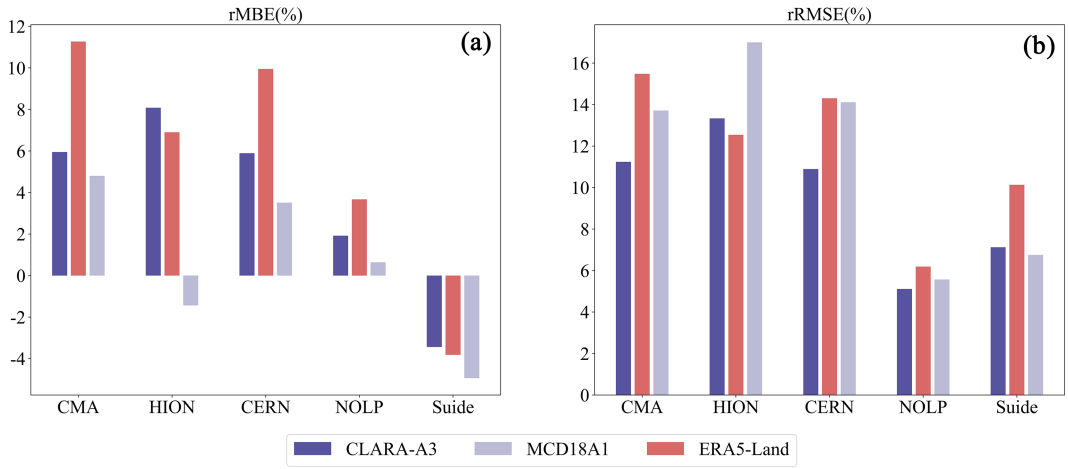

Fig. 6. Comparison of monthly DSR rMBE and rRMSE over different networks. (a) rMBE. (b) rRMSE.

E. Temporal Trend Consistency

To verify the accuracy of the three DSR products in representing the fluctuations and trends of the DSR time series, we utilized the average monthly DSR anomalies between January 2004 and December 2016 from 15 observed stations in the CMA network as comparative data to investigate the consistency of trend between three products and ground measurements. The results are shown in Fig. 8. CLARA-A3 and ERA5-Land captured fluctuations in DSR anomalies more accurately compared to MCD18A. In rectangle A with a dashed line in Fig. 8, MCD18A1 exhibits significant overestimation, whereas in rectangles B and C with a dashed line, there is a notable underestimation for MCD18A1. Especially in rectangle B in Fig. 8, the DSR anomalies from MCD18A1 in the year 2011 show a large bias, so we suggested that MCD81A1 DSR in 2011 should be carefully evaluated before applying over Loess Plateau. For the trend analysis, DSR anomalies of ground measurements

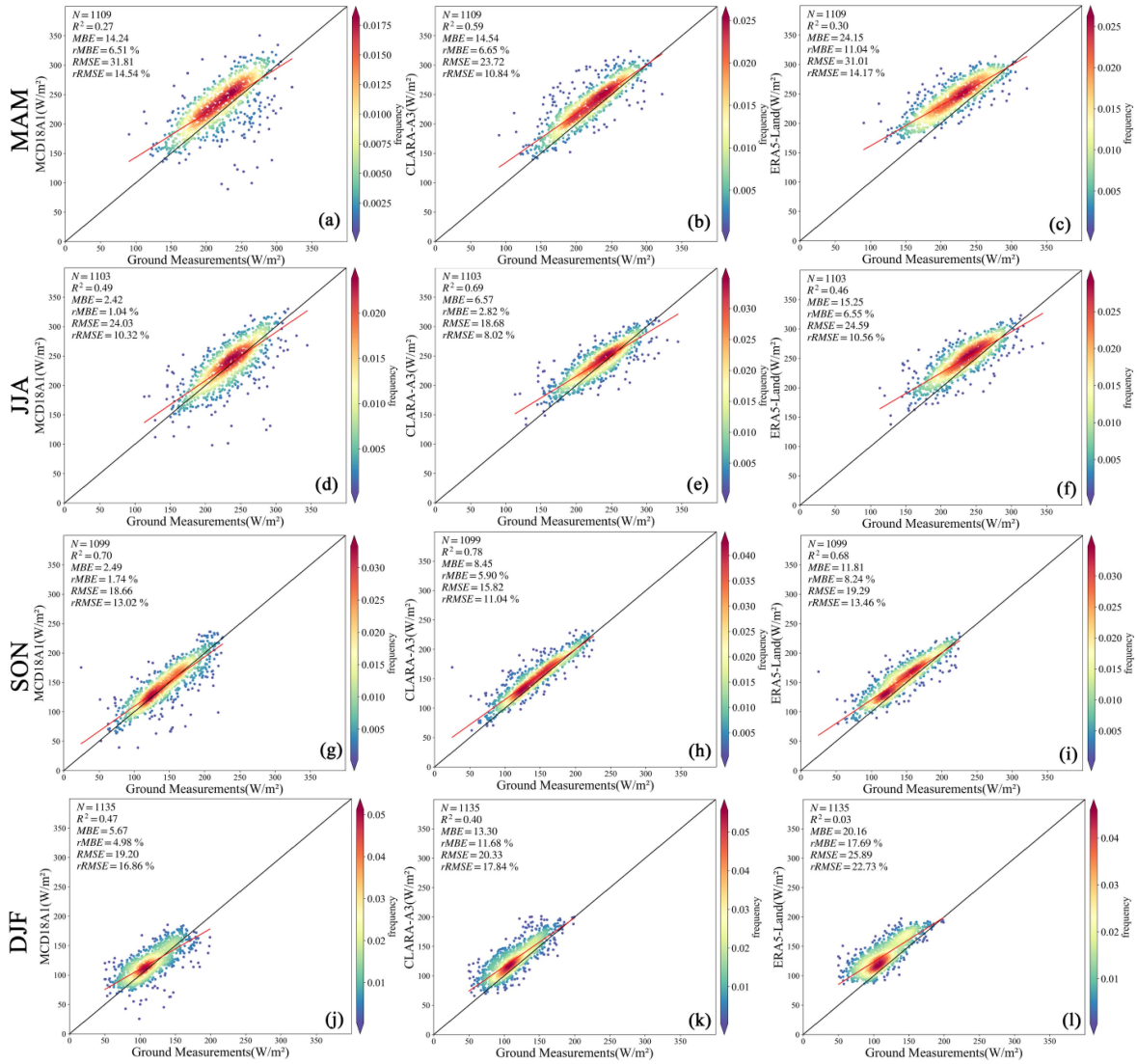

Fig. 7. Validation of seasonal DSR against ground measurements for MCD18A1, CLARA-A3 and ERA5-Land in (a-c) MAM, (d-f) JJA, (g-i) SON, and (j-l) DJF. Black line: 1:1 line. Red line: Fitted regression line.

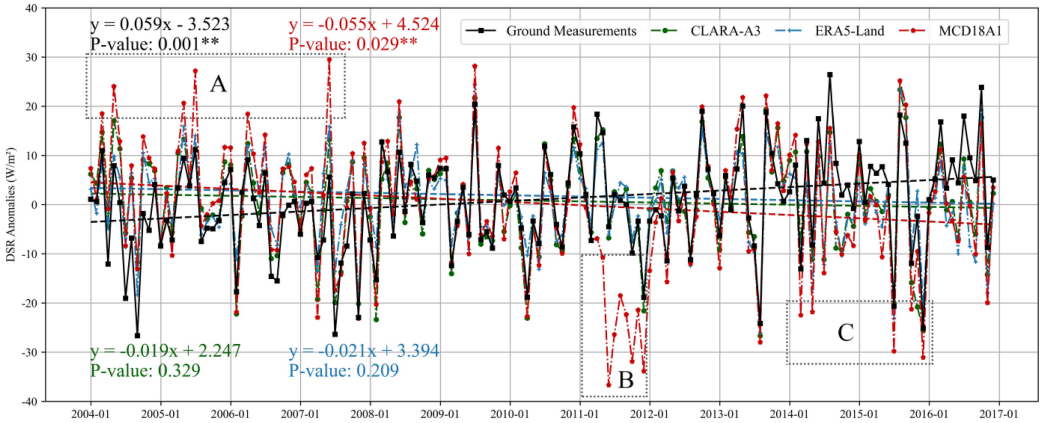

Fig. 8. Time series of monthly mean DSR anomalies of ground measurements and three DSR products from January 2004 to December 2016. The blank, green, blue, and red regression line and equation represent ground measurements, CLARA-A3, ERA5-land, and MCD18A1 (** marked as the significance level $p < 0.05$), respectively.

TABLE IV
MBE AND RMSE OF EACH PRODUCT AT DIFFERENT SPATIAL AND TEMPORAL RESOLUTIONS

Temporal scales	Products	25 km		10 km		1 km	
		MBE	RMSE	MBE	RMSE	MBE	RMSE
Monthly	CLARA-A3	10.46	19.31				
	ERA5-Land	17.66	25.36	17.82	25.37		
	MCD18A1	6.22	25.03	6.67	24.88	6.39	23.97
Daily	CLARA-A3	11.89	31.30				
	ERA5-Land	18.86	39.74	19.00	39.72		
	MCD18A1	7.15	46.14	7.26	45.36	6.92	44.40

Note: The units of MBE and RMSE are W/m^2.

exhibit a significant increasing trend during 2004 and 2016, whereas MCD18A1 exhibits a contrasting significant decreasing trend. While both CLARA-A3 and ERA5-Land show decreasing trends with no statistical significance. Therefore, three products can represent the fluctuation of DSR to some extent, except that MCD18A1 shows outliners with significant over or underestimation. For trend consistency, they show different trends with ground measurements. MCD18A1 shows an opposite trend with the ground measurements, whereas the decreasing trend of CLARA-A3 and ERA5-Land that are also opposite with ground measurements are relatively small and with no significance.

IV. DISCUSSION

A. Spatial Representativeness

The three products have different spatial resolutions. Product errors caused by spatial representativeness may introduce uncertainty in the validation of product accuracy. Therefore, it is important to verify product accuracy at different spatial resolutions and investigate the impact of the spatial aggregation process on different product accuracy. CLARA-A3 has the lowest resolution and therefore does not require aggregation, only validation at a 25-km scale. ERA5-Land accuracy validation was carried out at both 25 and 10-km resolutions. MCD18A1 underwent accuracy validation at three different resolutions. Accuracy validation results for the three products at different resolutions are listed in Table IV. In the process of aggregating to coarser resolutions, the accuracy of MCD18A1 decreases. When aggregated from 1 to 25 km, the RMSE of daily MCD18A1 DSR increases from 44.40 W/m^2 to 46.14 W/m^2, and MBE also increases from 6.92 to 7.15 W/m^2. The monthly RMSE increases from 23.97 to 25.03 W/m^2, with a rate of increase of 4.42%. When aggregated from 10 to 25 km, the accuracy of ERA5-Land almost no change. However, MCD18A1 shows a slight decrease in accuracy at daily and monthly scales. The daily RMSE of MCD18A1 increases from 45.36 to 46.14W/m^2. The monthly RMSE of MCD18A1 increases from 24.88 to 25.03 W/m^2. Previous studies have indicated that the accuracy of MCD18A1 products improves when aggregated from high resolution to low resolution [20], [33]. However, in this study, it was found that in the Loess Plateau and its surrounding areas, when MCD18A1 products are aggregated from high resolution to low resolution, the accuracy of the product actually decreases. This may be related to the complex terrain in the study area.

TABLE V
ERRORS UNDER TERRAIN WITH DIFFERENT SVFS

SVF	rRMSE			
	CLARA-A3	ERA5-Land	MCD18A1	Average
SVF>0.9	17.06%	22.66%	25.27%	21.66%
0.8<SVF<0.9	21.27%	22.80%	28.24%	24.10%
0.7<SVF<0.8	23.70%	25.25%	29.78%	26.24%
0.6<SVF<0.7	29.50%	28.04%	30.45%	29.33%

B. Errors Over the Areas With Different Terrain Reliefs

The Loess Plateau is characterized by rugged terrain with numerous gullies and ridges, resulting in a complex topography. As a consequence, solar radiation in this region is significantly affected by the terrain. However, during the production process of CLARA-A3, ERA5-Land, and MCD18A1, the influence of topography was not taken into consideration. Therefore, this study further investigates the impact of topographic factors on solar radiation products in the Loess Plateau and surrounding areas. We calculated Sky View Factor (SVF) which is the proportion of visible sky over the hemisphere for stations and SVF was calculated using viewshed in the Solar Analyst model in ArcGIS. The rRMSE of stations are categorized based on SVF, as shown in Table V. Due to the shielding effect of terrain features, there is a notable uncertainty in the amount of solar radiation reaching the ground. Therefore, if topographic factors are not considered in inversion algorithms or reanalysis models, there will be a significant error in the inversion and simulation results. Based on Table V, it can be observed that all three products have a lower rRMSE at stations with higher terrain openness compared to those with lower terrain openness which means higher accuracy for the product over relatively flat areas. Notably, for different products, when SVF $>$ 0.7, the CLERA-A3 exhibits superior accuracy over ERA5-Land and MCD18A1. However, it exhibits the highest sensitivity to topography. With SVF $>$ 0.9, the rRMSE reaches 17.06%. As terrain obstruction increases to 0.6 $<$ SVF $<$ 0.7, the rRMSE escalates to 29.50%. Therefore, in regions with complex terrain, it is imperative to consider topographic factors during remote sensing data retrieval and reanalysis processes.

C. Snow Effect on Accuracy of DSR Products

Snow, as a high albedo surface, introduces two potential reasons for significant errors in DSR in snow-covered regions. The surface albedo would be mistaken if the snow cover area was misclassified which consequently reduced the accuracy of the DSR products. Second, the albedo of snow is similar to

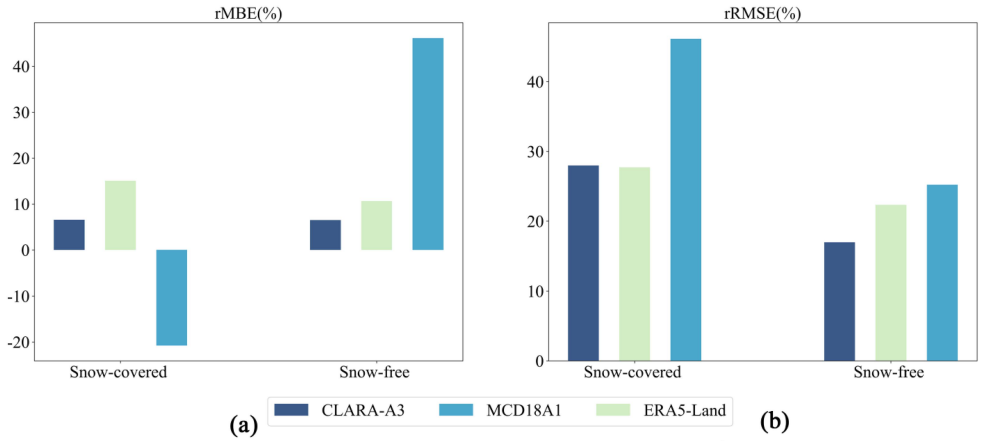

Fig. 9. Comparison of the rMBE and rRMSE over snow-covered and snow-free areas. (a) rMBE. (b) rRMSE.

that of clouds which could potentially lead to misidentification, which leads to large errors for satellite DSR. To verify the influence of snow cover on DSR products, we employed the China AVHRR Daily Cloudless 5 km Snow Area Product Dataset [40] to distinguish between snow-covered and snow-free areas. Fig. 9 shows a comparison of the accuracy of the three products in snow-covered and snow-free areas. Due to the influence of snow cover, the accuracy of all three products is reduced. MCD18A1 is most significantly affected by snow cover, exhibiting a substantial underestimation of DSR (rMBE: −20.77%) in snow-covered areas. The rRMSE in the snow-covered area is 46.15%, which is 20.93% higher than that in snow-free areas. In snow-covered areas, CLARA-A3 and ERA5-Land have rRMSE of 27.98% and 27.72%, respectively, representing increases of 11.01% and 5.38% compared to snow-free areas. ERA5's surface albedo, is used as input data for generating CLARA-A3, which is the possible reason for their similar performance over snow-covered areas. Comparing the rRMSE of three products over snow-covered areas, we can conclude that CLARA-A3 and ERA5-Land are less affected by snow cover.

V. Conclusion

In this study, we assessed the DSR data derived from satellite products CLARA-A3 and MCD18A1, as well as the most recent ECMWF reanalysis dataset ERA5-Land. The evaluation encompassed various temporal scales, ranging from intraday to daily, monthly, and seasonal intervals. The temporal trends consistency between products and ground measurements were also evaluated. Furthermore, we delved into potential factors contributing to discrepancies in DSR product accuracy.

We evaluated the 3-h and instantaneous DSR of MCD18A1 at the original resolution, as well as the 1-h DSR of ERA5-Land. The MBE for instantaneous and 3-h DSR of MCD18A1 were -6.88 W/m^2 and -1.76 W/m^2, respectively, both indicating a tendency toward underestimation. In contrast, the ERA5-Land 1-h DSR showed a severe overestimation with an MBE of 37.26 W/m^2. The RMSE of ERA5-Land 1-h DSR is significantly higher in the Loess Plateau (169.74 W/m^2) than in China where the RMSE is 120.2 W/m^2. CLARA-A3 demonstrated consistent performance on daily and monthly scales and outperformed the other two products. MCD18A1 performed better than ERA5-Land on a daily scale, but the accuracy of the two products was similar on a monthly scale. Evaluation of temporal trend consistency between products and ground measurements was also carried out in monthly DSR. MCD18A1 shows an opposite trend with the ground measurements, whereas the decreasing trend of CLARA-A3 and ERA5-Land that are also opposite with ground measurements are relatively small and with no significance.

Furthermore, we explored potential factors contributing to significant errors in DSR products. First, we discussed the influence of spatial representativeness. In the Loess Plateau characterized by complex terrain, the satellite product MCD18A1 with a spatial resolution of 1 km showed a decrease in accuracy when aggregated to coarser resolutions. In contrast, reanalysis data ERA5-Land with a resolution of 10 km maintained consistent accuracy when aggregated to 25 km. Then, we examined the influence of topography on product accuracy under different SVFs. The results indicated that the rRMSE of DSR products increased with greater terrain obstruction. Among the products, CLARA-A3 displayed the highest sensitivity to topographic influence. Finally, we investigated the impact of snow cover on DSR products using corresponding data. Here, it was evident that MCD18A1 was significantly affected by snow cover.

In summary, CLARA-A3 showed higher accuracy than ERA5-Land and MCD18A1 over the Loess Plateau on daily and monthly scales. However, the error of CLARA-A3 is sensitive to terrain effects. In practical applications, especially in areas with flat terrain and without considering spatial resolution, CLARA-A3 is the better choice. When a higher-resolution DSR product is needed, MCD18A1 with a spatial resolution of 1 km can be considered. But MCD18A1 demonstrated an opposite temporal trend to ground measurements and showed a large deviation in the year 2011. So, we suggested that MCD81A1 DSR in 2011 should be carefully evaluated before applying over the Loess Plateau. All findings can be references for DSR product selection over Loess Plateau.

APPENDIX

TABLE VI
LIST OF ACRONYMS

Acronym	Full name
BESS	Breathing Earth System Simulator
BSRN	Baseline Surface Radiation Network
CERES	The Clouds and the Earth's Radiant Energy System
CERES-EBAF	The Clouds and the Earth's Radiant Energy System-Energy Balanced and Filled
CERES-SYN	The Clouds and the Earth's Radiant Energy System-Synoptic
CFSR	Climate Forecast System Reanalysis
CFSv2	Climate Forecast System Reanalysis Edition 2 data
CLARA-A3	CLoud, Albedo and surface Radiation dataset from AVHRR Edition 3 data
CMA	Chinese Meteorological Administration
DAM	Multi-layer Simulation and Data Assimilation Center of the Tibetan Plateau
DSR	Downward Shortwave Radiation
ECMWF	European Centre for Medium-Range Weather Forecasts
ERA5	Fifth generation European Centre for Medium-Range Weather Forecasts Reanalysis
ERA5-Land	Land component of the Fifth generation European Centre for Medium-Range Weather Forecasts Reanalysis
ERA-Interim	European Centre for Medium-Range Weather Forecasts Interim Re-Analysis
FMI	Finnish Meteorological Institute
FY-2C	Feng Yun 2C
GAME-Tibet	GEWEX Asian Monsoon Experiments-Tibet
GC-NET	Greenland Climate Network
GEBA	Global Energy Balance Archive
GEWEX	Global Energy and Water Cycle Experiment
GEWEX-SRB	Global Energy and Water Cycle Experiment-Surface Radiation Budget
GLASS-DSR	Global Land Surface Satellite-DSR
ISCCP	International Satellite Cloud Climatology Project
ISCCP-FD	International Satellite Cloud Climatology Project-Flux Data
MBE	Mean Bias Error
MCD18	Moderate Resolution Imaging Spectroradiometer land surface DSR
MODIS	Moderate Resolution Imaging Spectroradiometer
MERRA	Modern-Era Retrospective Analysis for Research and Applications
NCEP	National Centers for Environmental Prediction
NCEP-DOR	the National Centers for Environmental Prediction–Department of Energy
NCEP-NCAR	National Centers for Environmental Prediction–National Center for Atmospheric Research
NIBIO	Institute of Bioeconomy Research for emergency services and agricultural research
NOAA	National Oceanic and Atmospheric Administration
NSMC	National Satellite Meteorological Centre
R^2	The coefficient of determination
RMSE	Root Mean Square Error
SVF	Sky View Factor
UMD	University of Maryland
UMD-SRB	University of Maryland-Surface Radiation Budget

REFERENCES

[1] S. Liang, K. Wang, X. Zhang, and M. Wild, "Review on estimation of land surface radiation and energy budgets from ground measurement, remote sensing and model simulations," *IEEE J. Sel. Topics Appl. Earth Observ. Remote Sens.*, vol. 3, no. 3, pp. 225–240, Sep. 2010, doi: 10.1109/JSTARS.2010.2048556.

[2] S. Liang, D. Wang, T. He, and Y. Yu, "Remote sensing of Earth's energy budget: Synthesis and review," *Int. J. Digit. Earth*, vol. 12, no. 7, pp. 737–780, Mar. 2019, doi: 10.1080/17538947.2019.1597189.

[3] S. Niemelä, P. Räisänen, and H. Savijärvi, "Comparison of surface radiative flux parameterizations: Part II. Shortwave radiation," *Atmos. Res.*, vol. 58, no. 2, pp. 141–154, Jul. 2001, doi: 10.1016/S0169-8095(01)00085-0.

[4] C. A. Gueymard, "A review of validation methodologies and statistical performance indicators for modeled solar radiation data: Towards a better bankability of solar projects," *Renewable Sustain. Energy Rev.*, vol. 39, pp. 1024–1034, Nov. 2014, doi: 10.1016/j.rser.2014.07.117.

[5] H. Jiang, N. Lu, J. Qin, W. Tang, and L. Yao, "A deep learning algorithm to estimate hourly global solar radiation from geostationary satellite data," *Renewable Sustain. Energy Rev.*, vol. 114, Oct. 2019, Art. no. 109327, doi: 10.1016/j.rser.2019.109327.

[6] H. Yan, J. Huang, P. Minnis, T. Wang, and J. Bi, "Comparison of CERES surface radiation fluxes with surface observations over Loess Plateau," *Remote Sens. Environ.*, vol. 115, no. 6, pp. 1489–1500, Jun. 2011, doi: 10.1016/j.rse.2011.02.008.

[7] T. Zhang, P. W. Stackhouse, S. K. Gupta, S. J. Cox, J. Colleen Mikovitz, and L. M. Hinkelman, "The validation of the GEWEX SRB surface shortwave flux data products using BSRN measurements: A systematic quality control, production and application approach," *J. Quant. Spectrosc. Radiative Transf.*, vol. 122, pp. 127–140, Jun. 2013, doi: 10.1016/j.jqsrt.2012.10.004.

[8] H. Han, G. Y. Ren, W. Wang, L. H. Zhu, Z. H. Wu, and H. Y. Zhang, "Temporal and spatial variation characteristics of total solar radiation over the Loess Plateau region," *Climatic Environ. Res.*, vol. 13, no. 1, pp. 61–66, Jan. 2008, doi: 10.3878/j.issn.1006-9585.2008.01.08.

[9] H. Letu et al., "A review of the estimation of downward surface shortwave radiation based on satellite data: Methods, progress and problems," *Sci. China Earth Sci.*, vol. 63, no. 6, pp. 774–789, Apr. 2020, doi: 10.1007/s11430-019-9589-0.

[10] A. H. Young, K. R. Knapp, A. Inamdar, W. Hankins, and W. B. Rossow, "The international satellite cloud climatology project H-series climate data record product," *Earth Syst. Sci. Data*, vol. 10, no. 1, pp. 583–593, Mar. 2018, doi: 10.5194/essd-10-583-2018, 2018.

[11] A. K. Betts, M. Zhao, P. A. Dirmeyer, and A. C. M. Beljaars, "Comparison of ERA40 and NCEP/DOE near-surface data sets with other ISLSCP-II data sets," *J. Geophy. Res., Atmos.*, vol. 111, Aug. 2006, Art. no. D22S04, doi: 10.1029/2006JD007174.

[12] M. Wild, "Global dimming and brightening: A review," *J. Geophy. Res., Atmos.*, vol. 114, no. D10, Jun. 2009, Art. no. D00D16, doi: 10.1029/2008JD011470.

[13] D. A. Rutan et al., "CERES synoptic product: Methodology and validation of surface radiant flux," *J. Atmos. Ocean. Technol.*, vol. 32, no. 6, pp. 1121–1143, Jun. 2015, doi: 10.1175/JTECH-D-14-00165.1.

[14] U. Pfeifroth, A. Sanchez-Lorenzo, V. Manara, J. Trentmann, and R. Hollmann, "Trends and variability of surface solar radiation in Europe based on surface-and satellite-based data records," *J. Geophy. Res., Atmos.*, vol. 123, no. 3, pp. 1735–1754, Jan. 2018, doi: 10.1002/2017JD027418.

[15] D. Wang, S. Liang, Y. Zhang, X. Gao, M. G. L. Brown, and A. Jia, "A new set of MODIS land products (MCD18): Downward shortwave radiation and photosynthetically active radiation," *Remote Sens.*, vol. 12, no. 1, Jan. 2020, Art. no. 168, doi: 10.3390/RS12010168.

[16] K. G. Karlsson et al., "CLARA-A3: The third edition of the AVHRR-based CM SAF climate data record on clouds, radiation and surface albedo covering the period 1979 to 2023," *Earth Syst. Sci. Data*, vol. 15, no. 11, pp. 4901–4926, Nov. 2023, doi: 10.5194/essd-2023-133.

[17] X. Deng, P. Zhai, and C. Yuan, "Comparison and analysis of several sets of foreign reanalysis data," *Meteorol. Sci. Technol.*, vol. 38, no. 1, pp. 1–8, 2010, doi: 10.19517/j.1671-6345.2010.01.001.

[18] X. Zhang, S. Liang, G. Wang, Y. Yao, B. Jiang, and J. Cheng, "Evaluation of the reanalysis surface incident shortwave radiation products from NCEP, ECMWF, GSFC, and JMA using satellite and surface observations," *Remote Sens.*, vol. 8, no. 3, Mar. 2016, Art. no. 225, doi: 10.3390/rs8030225.

[19] X. Zhang, S. Liang, M. Wild, and B. Jiang, "Analysis of surface incident shortwave radiation from four satellite products," *Remote Sens. Environ.*, vol. 165, pp. 186–202, Aug. 2015, doi: 10.1016/j.rse.2015.05.015.

[20] R. Li, D. Wang, and S. Liang, "Comprehensive assessment of five global daily downward shortwave radiation satellite products," *Sci. Remote Sens.*, vol. 4, Dec. 2021, Art. no. 100028, doi: 10.1016/j.srs.2021.100028.

[21] X. Zhang, N. Lu, H. Jiang, and L. Yao, "Evaluation of reanalysis surface incident solar radiation data in China," *Sci. Rep.*, vol. 10, no. 1, Feb. 2020, Art. no. 3494, doi: 10.1038/s41598-020-60460-1.

[22] J. Zhang, R. Shen, C. Shi, L. Bai, J. Liu, and S. Sun, "Evaluation and comparison of downward solar radiation from new generation atmospheric reanalysis ERA5 across mainland China," *J. Geo-Inf. Sci.*, vol. 23, no. 12, pp. 2261–2274, Dec. 2021, doi: 10.12082/dqxxkx.2021.180357.

[23] B. Jia, Z. Xie, A. Dai, C. Shi, and F. Chen, "Evaluation of satellite and reanalysis products of downward surface solar radiation over East Asia: Spatial and seasonal variations," *J. Geophy. Res., Atmos.*, vol. 118, no. 9, pp. 3431–3446, Mar. 2013, doi: 10.1002/jgrd.50353.

[24] K. Yang, T. Koike, P. Stackhouse, C. Mikovitz, and S. J. Cox, "An assessment of satellite surface radiation products for highlands with Tibet instrumental data," *Geophy. Res. Lett.*, vol. 33, no. 22, Nov. 2006, Art. no. L22403, doi: 10.1029/2006GL027640.

[25] K. Yang et al., "Evaluation of satellite estimates of downward shortwave radiation over the Tibetan Plateau," *J. Geophys. Res., Atmos.*, vol. 113, no. D17, Sep. 2008, Art. no. D17204, doi: 10.1029/2007JD009736.

[26] A. Wang and X. Zeng, "Evaluation of multireanalysis products with in situ observations over the Tibetan Plateau," *J. Geophy. Res., Atmos.*, vol. 117, no. D5, Mar. 2012, Art. no. D05102, doi: 10.1029/2011JD016553.

[27] Q. Shi and S. Liang, "Characterizing the surface radiation budget over the Tibetan Plateau with ground-measured, reanalysis, and remote sensing data sets: 1. Methodology," *J. Geophys. Res., Atmos.*, vol. 118, no. 16, pp. 9642–9657, Aug. 2013, doi: 10.1002/jgrd.50720.

[28] Q. Zhang, L. Zhang, J. Huang, L. Y. Zhang, W. Wang, and S. Sha, "Spatial distribution of surface energy fluxes over the Loess Plateau in China and its relationship with climate and the environment," *Sci. China Earth Sci.*, vol. 57, pp. 2135–2147, May 2014, doi: 10.1007/s11430-014-4881-9.

[29] N. Wang et al., "Magnitude of soil erosion in small catchments with different land use patterns under an extreme rainstorm event over the Northern Loess Plateau, China," *CATENA*, vol. 195, Dec. 2020, Art. no. 104780, doi: 10.1016/j.catena.2020.104780.

[30] F. Jin, W. Yang, J. Fu, and Z. Li, "Effects of vegetation and climate on the changes of soil erosion in the Loess Plateau of China," *Sci. Total Environ.*, vol. 773, Jun. 2021, Art. no. 145514, doi: 10.1016/j.scitotenv.2021.145514.

[31] Y. Zhang, W. B. Rossow, A. A. Lacis, V. Oinas, and M. I. Mishchenko, "Calculation of radiative fluxes from the surface to top of atmosphere based on ISCCP and other global data sets: Refinements of the radiative transfer model and the input data," *J. Geophys. Res., Atmos.*, vol. 109, no. D19, Oct. 2004, Art. no. D19105, doi: 10.1029/2003JD004457.

[32] Y. Ma and R. T. Pinker, "Modeling shortwave radiative fluxes from satellites," *J. Geophys. Res., Atmos.*, vol. 117, no. D23, Oct. 2012, Art. no. D23202, doi: 10.1029/2012JD018332.

[33] L. Tong, T. He, Y. Ma, and X. Zhang, "Evaluation and intercomparison of multiple satellite-derived and reanalysis downward shortwave radiation products in China," *Int. J. Digit. Earth*, vol. 16, no. 1, pp. 1853–1884, May 2023, doi: 10.1080/17538947.2023.2212918.

[34] F. Wu and C. Fu, "Assessment of GEWEX/SRB version 3.0 monthly global radiation dataset over China," *Meteorol. Atmos. Phys.*, vol. 112, pp. 155–166, Apr. 2011, doi: 10.1007/s00703-011-0136-x.

[35] H. Jiang, Y. Yang, Y. Bai, and H. Wang, "Evaluation of the total, direct, and diffuse solar radiations from the ERA5 reanalysis data in China," *IEEE Geosci. Remote Sens. Lett.*, vol. 17, no. 1, pp. 47–51, Jan. 2020, doi: 10.1109/LGRS.2019.2916410.

[36] R. W. Mueller, C. Matsoukas, A. Gratzki, H. D. Behr, and R. Hollmann, "The CM-SAF operational scheme for the satellite based retrieval of solar surface irradiance — A LUT based eigenvector hybrid approach," *Remote Sens. Environ.*, vol. 113, no. 5, pp. 1012–1024, May 2009, doi: 10.1016/j.rse.2009.01.012.

[37] J. Muñoz-Sabater et al., "ERA5-land: A state-of-the-art global reanalysis dataset for land applications," *Earth Syst. Sci. Data*, vol. 13, no. 9, pp. 4349–4383, Sep. 2021, doi: 10.5194/essd-13-4349-2021.

[38] A. Roesch, M. Wild, A. Ohmura, E. G. Dutton, C. N. Long, and T. Zhang, "Assessment of BSRN radiation records for the computation of monthly means," *Atmos. Meas. Techn.*, vol. 4, no. 2, pp. 339–354, Feb. 2011, doi: 10.5194/amt-4-339-2011.

[39] B. Espinar, P. Blanc, L. Wald, C. Hoyer-Lick, M. Schroedter-Homscheidt, and T. Wanderer, "Controlling the quality of measurements of meteorological variables and solar radiation. From sub-hourly to monthly average time periods," EGU Gen. Assembly, European Geosciences Union, Vienna, Austria, 2012.

[40] X. Hao et al., "The NIEER AVHRR snow cover extent product over China – A long-term daily snow record for regional climate research," *Earth Syst. Sci. Data*, vol. 13, no. 10, pp. 4711–4726, Oct. 2021, doi: 10.5194/essd-13-4711-2021.

Qianqian Tian received the B.E. degree in remote sensing science and technology in 2020 from Xi'an University of Science and Technology, Xi'an, China, where she is currently working toward the M.Sc. degree in geomatics.

Her current research focuses on the generation of solar radiation products with high spatial and temporal resolution over Loess Plateau.

Shuhua Zhang received the B.S. degree in mathematics and applied mathematics from Shihezi University, Shihezi, China, in 2011, and the Ph.D. degree in physical geography from the Chinese Academy of Sciences, Beijing, China, in 2016.

She is currently an Associate Professor with Xi'an University of Science and Technology, Xi'an, China. Her current research focuses on the estimation of surface shortwave radiation over complex terrain.

Weili Duan received the B.E. degree in chemical engineering from Sichuan University, Chengdu, China, in 2008, and the Ph.D. degree in civil engineering and earth resources from Kyoto University, Kyoto, Japan, in 2014.

He is currently a Professor with Xinjiang Institute of Ecology and Geography, Chinese Academy of Sciences, Urumqi, China. His research interests include sustainable utilization of water resources, hydrological processes of land surface, global climate change, assessment of water pollution, and management of water disasters.

Guanghui Ming received the Ph.D. degree in hydraulic engineering from Tsinghua University, Beijing, China, in 2018.

He is currently a Senior Engineer with Yellow River Engineering Consulting Company Ltd., Zhengzhou, China. His research interests include efficient use and optimal allocation of water resources in arid areas, carbon-water coupling, and soil water-salt transport in oasis farmland ecosystems.